RSC Advances

PAPER

View Article Online
View Journal | View Issue

Cite this: *RSC Adv.*, 2023, **13**, 15606

Theoretical investigation of CO_2 capture in the MIL-88 series: effects of organic linker modification†

Nguyen Thi Xuan Huynh,[a] Ong Kim Le,[bc] Tran Phuong Dung,[cd] Viorel Chihaia[e] and Do Ngoc Son *[bc]

Received 10th March 2023
Accepted 13th May 2023

DOI: 10.1039/d3ra01588b

rsc.li/rsc-advances

CO_2 capture is a crucial strategy to mitigate global warming and protect a sustainable environment. Metal–organic frameworks with large surface area, high flexibility, and reversible adsorption and desorption of gases are good candidates for CO_2 capture. Among the synthesized metal–organic frameworks, the MIL-88 series has attracted our attention due to their excellent stability. However, a systematic investigation of CO_2 capture in the MIL-88 series with different organic linkers is not available. Therefore, we clarified the topic *via* two sections: (1) elucidate physical insights into the CO_2@MIL-88 interaction by van der Waals-dispersion correction density functional theory calculations, and (2) quantitatively study the CO_2 capture capacity by grand canonical Monte Carlo simulations. We found that the $1\pi_g$, $2\sigma_u/1\pi_u$, and $2\sigma_g$ peaks of the CO_2 molecule and the C and O p orbitals of the MIL-88 series are the predominant contributors to the CO_2@MIL-88 interaction. The MIL-88 series, *i.e.*, MIL-88A, B, C, and D, has the same metal oxide node but different organic linkers: fumarate (MIL-88A), 1,4-benzene-dicarboxylate (MIL-88B), 2,6-naphthalene-dicarboxylate (MIL-88C), and 4,4′-biphenyl-dicarboxylate (MIL-88D). The results exhibited that fumarate should be the best replacement for both the gravimetric and volumetric CO_2 uptakes. We also pointed out a proportional relationship between the capture capacities with electronic properties and other parameters.

1 Introduction

The energy consumption activities of industries, vehicles, and daily demands intensively depend on fossil fuels and natural gases. The by-products of such processes contain harmful emissions, especially CO_2, a greenhouse gas related to the global warming phenomenon.[1] Also, there is a huge amount of CO_2 emitted by agricultural activities and forest exploitation and reclamation.[2] For sustainable environment and energy usage, CO_2 capture and reduction are indispensable. Until now, post-combustion (mainly used in coal-gasification plants), pre-combustion, and oxyfuel combustion (primarily used in gas and coal-fired plants) have been crucial technologies for carbon capture.[3] However, these technologies face many challenges such as CO_2 separation and purification from flue gas streams and gas mixtures.[4] The solution to these problems is searching for solid materials that meet the requirements,[5] *i.e.*, high adsorption capacity, high selectivity, fast adsorption and desorption, and durability for CO_2 capture based on adsorption effects.[6–8] Solid sorbents that have been used to adsorb CO_2 include rigid classical adsorbents (activated carbon and zeolites) and novel porous adsorbents (covalent organic frameworks, zeolitic imidazolate frameworks, and metal–organic frameworks). Nowadays, metal–organic frameworks (MOFs)[9,10] have become the most popular CO_2 capture material due to their many outstanding features: ultra-large surface area, high porosity, and remarkable chemical, thermal, and mechanical stabilities.[11,12]

So far, MOF-200 and MOF-210 recorded the highest capacity for the gravimetric CO_2 uptake of 2400 mg g^{-1} (74.2 wt%) and 2396 mg g^{-1} (73.9 wt%) at 298 K and 50 bar.[13] At the same condition of the temperature and pressure, MOF-117 was the best sorbent among the considered MOFs with the gravimetric and volumetric CO_2 uptakes of 33.5 mmol g^{-1} and 320 cm^3 (STP) per cm^3, respectively.[14] Besides, MIL-100(Cr) and MIL-101c(Cr) also achieved 18 mmol g^{-1} and 40 mmol g^{-1} (280 cm^3 (STP) per cm^3 and 390 cm^3 (STP) per cm^3 for volumetric loading) at 304 K and 50 bar; MIL-47(V) with 11 mmol g^{-1} and 250 cm^3 (STP) per cm^3 at 302 K, 20 bar, IRMOF-1 with 21.7 mmol g^{-1} and 290 cm^3 (STP) per cm^3 at 298 K, 35 bar.[15]

[a]*Faculty of Natural Sciences, Quy Nhon University, 170 An Duong Vuong, Quy Nhon City, Binh Dinh Province, Vietnam*

[b]*Ho Chi Minh City University of Technology (HCMUT), 268 Ly Thuong Kiet Street, District 10, Ho Chi Minh City, Vietnam. E-mail: dnson@hcmut.edu.vn*

[c]*Vietnam National University Ho Chi Minh City, Linh Trung Ward, Ho Chi Minh City, Vietnam*

[d]*Department of Chemistry, University of Science, Ho Chi Minh City, Vietnam*

[e]*Institute of Physical Chemistry "Ilie Murgulescu" of the Romanian Academy, Splaiul Independentei 202, Sector 6, 060021 Bucharest, Romania*

† Electronic supplementary information (ESI) available: Theoretical investigation of CO_2 capture in the MIL-88 series: effects of organic linker modification. See DOI: https://doi.org/10.1039/d3ra01588b

Other MOFs were also investigated for CO_2 capture as NU-100 (69.8 wt%, at 298 K and 40 bar), Mg-MOF-74 (68.9 wt%, at 278 K and 36 bar), MOF-5 (58 wt%, at 273 K and 10 bar), and HKUST-1 (19.8 wt%, 298 K and 1 bar).[16]

Among the successfully synthesized MOFs, the MIL-88 series have attracted our attention due to their exceptionally high flexibility and stability that MIL-88 series could swell upon immersion in various liquids with reversible variations in unit cell volume from 85% (MIL-88A) to 240% (MIL-88D) depending on the nature and length of the organic spacer without breaking the bonds, and fully retains its open framework topology.[17] Therefore, the MIL-88 series became a good candidate for CO_2 capture. In reality, MIL-88A(Fe) has been studied for catalysis,[18,19] NO adsorption,[20] and drug transportation.[21] Besides, MIL-88s (s = A, B, C, D) were investigated for hydrogen storage.[22–24] In 2016, the experiment measured CO_2 sorption capacity of MIL-88A as a function of temperatures, and the value achieved was 4.95 mmol g^{-1} at 30 °C and the pressure of 1 bar.[25] MIL-88 family has been synthesized by experiment,[26,27] where the structure of MIL-88A, B, C, and D has the same metal site but different organic linkers, *i.e.*, fumarate, 1,4-benzene-dicarboxylate, 2,6-naphthalene-dicarboxylate, and 4,4′-biphenyl-dicarboxylate, respectively. However, no research is available to systematically investigate the CO_2 capture capacity in the MIL-88 series and the physical meanings of the CO_2-MOF interaction under the influences of replacing organic linkers. Therefore, we elucidated these topics in the present work using the van der Waals dispersive correction density functional theory calculations for the earlier *via* electronic structure properties and the grand canonical Monte Carlo simulations for the later *via* adsorption isotherms, and isosteric heat of adsorption for the pressures below 100 bar. Elucidating the effects of defects and structural flexibility is out of the scope of the current work.

2 Computational techniques

2.1. Density functional theory calculations

We used the van der Waals dispersive correction density functional theory (vdW-DF) calculations with the revPBE-based exchange–correlation energy[28,29] *via* the Vienna Ab initio Simulation Package (VASP).[30,31] The projector augmented-wave technique was used to describe the electron–ion interactions and a cut-off energy of 700 eV for the plane-wave basis set.[32,33] The first Brillouin zone was sampled with a special *k*-point mesh of 3 × 3 × 3 for MIL-88A and B, 3 × 3 × 2 for MIL-88C and D, centred at the Gamma point following the Monkhorst–Pack method. The Methfessel–Paxton smearing of order 1 with the smearing width of 0.1 eV was used to support the convergence speed of geometry relaxation and the electronic density of states (DOS).[34] Besides, the tetrahedron method with the Bloch corrections has been selected for the total energy calculations.[35] Because the magnetic moments of the iron atom of the MIL-88 series are inconsistent with the spin-polarized calculations due to the structural flexibility, we, therefore, performed the non-spin polarized scheme in the present study. The structure and unit cell of the MIL-88 series are shown in Fig. 1. MIL-88A, B, C, and D share the same metal oxide node (Fe_3O) but different ligands, *i.e.*, fumarate or FMA (OOC–C_2H_2–COO), 1,4-benzene-dicarboxylate or BDC (OOC–C_6H_4–COO), 2,6-naphthalene-dicarboxylate or NDC (OOC–$C_{10}H_6$–COO), and 4,4′-biphenyl-dicarboxylate or BPDC (OOC–$C_{12}H_8$–COO), respectively.

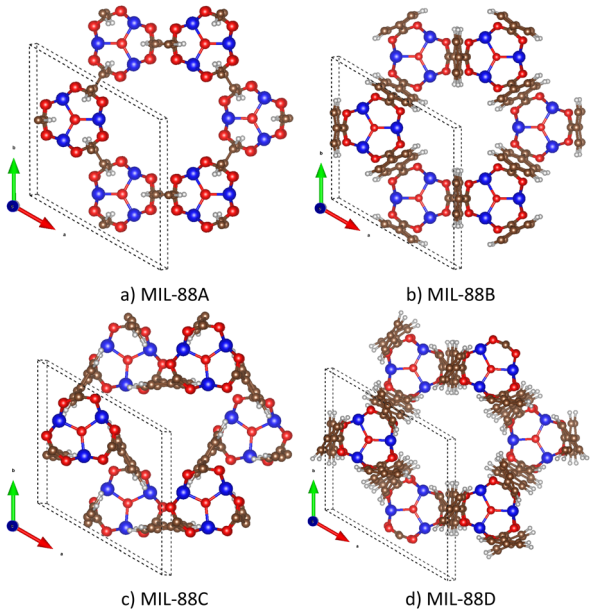

Fig. 1 The structure of MIL-88 series. The dotted frame indicates the unit cell. Fe (blue), O (red), and C (brown), and H (light-grey).

Before exploring the CO_2 adsorption configurations, we have to fully optimize the atomic positions and the unit cell volume of the MIL-88 series, which followed the procedure of our previous publications.[22,23] We then carried out the geometric optimization to search for the CO_2 adsorption configurations and favorable sites. The adsorption energy of the CO_2 molecule in the MIL-88 series was calculated by

$$\Delta E_{ads} = E_{MIL+CO_2} - (E_{MIL} + E_{CO_2}), \quad (1)$$

where $E_{MIL+CO2}$, E_{MIL}, and E_{CO_2} are the total energy of the [MIL-88 + CO_2] system, the pristine MIL-88, and the isolated CO_2 molecule, respectively. Besides, we calculated the charge density difference of the [MIL-88 + CO_2] system *via* the expression

$$\Delta\rho = \rho_{MIL+CO_2} - (\rho_{MIL} + \rho_{CO_2}), \quad (2)$$

here ρ_{MIL+CO_2}, ρ_{MIL}, and ρ_{CO_2} are the charge density of the [MIL-88 + CO_2] system, the pristine MIL-88, and the isolated CO_2 molecule, respectively.

2.2. Grand canonical Monte Carlo simulations

After optimizing the volume and structure of the MIL-88 series, we obtained the charge distribution in the unit cell. We then used the density-derived electrostatic and chemical charge (DDEC6) method[36–39] to calculate the partial point charge for the atoms of the MIL-88 series. This charge assignment was used to parameterize the force fields as follows.

The interaction between the CO_2 molecule and the MIL-88 series was modelled by

$$U(r_{ij}) = U_{vdW}(r_{ij}) + U_{elec}(r_{ij}), \quad (3)$$

where r_{ij} is the distance between the i^{th} and j^{th} atoms. The above interaction consists of two parts:

(i) The van der Waals (vdW) interaction was described by the Lennard-Jones (LJ) potential,

$$U_{vdW}(r_{ij}) = 4\varepsilon_{ij}\left[\left(\frac{\sigma_{ij}}{r_{ij}}\right)^2 - \left(\frac{\sigma_{ij}}{r_{ij}}\right)^6\right], \quad (4)$$

where, the parameters ε_{ij} and σ_{ij} are the Lennard-Jones (LJ) potential well depth and diameter, respectively. These parameters were determined by the Lorentz–Berthelot mixing rule for a pair of unlike atoms:

$$\varepsilon_{ij} = \sqrt{\varepsilon_i \varepsilon_j} \text{ and } \sigma_{ij} = \frac{\sigma_i + \sigma_j}{2}, \quad (5)$$

here, σ_i and ε_i (i = the Fe, H, C, O atoms of MIL-88A, B, C, and D) were taken from the generic force fields for MOFs.[40] Notice that the cutoff radius of 22 Å has been checked for the convergence of the vdW interaction.

(ii) The electrostatic interaction with a cutoff radius of 13 Å,

$$U_{elec}(r_{ij}) = \frac{1}{4\pi\varepsilon_0}\frac{q_i q_j}{r_{ij}}. \quad (6)$$

Here, ε_0 is the dielectric constant of the vacuum, and q_i is the partial charge of the i^{th} atom, which was obtained by the DDEC6 method.[36–39] The atomic charge of the atoms in the MIL-88 series was listed in Table 1.[23] Where, Fe, H, C1, C2, C3, C4, C5, O1, and O2 were also displayed in Fig. 2. The force field parameters for the CO_2 molecule were described as a rigid three-site molecule using the EPM2 model (elementary physical model).[41,42]

With the obtained force fields, we carried out the GCMC simulations using the RASPA code[40] to calculate the CO_2 adsorption isotherms in the MIL-88 series with μVT ensembles (*i.e.*, fixed the temperature, volume, and chemical potential) for various pressures up to 60 bar and 298 K (room temperature). In the GCMC simulation process, the MIL-88 series was kept fixed while the CO_2 molecule could move by inserting, translating, rotating, and deleting operations. We obtained the total (n_{tot}) and excess (n_{exc}) uptakes of CO_2, satisfying the relationship

$$n_{exc} = n_{tot} - V_g\rho_g. \quad (7)$$

Here, V_g and ρ_g are the pore volume of the MIL-88 and the molar density of the bulk gas phase, respectively.

To evaluate the strength of the adsorbate–adsorbent interaction within the GCMC simulations, the total heat of adsorption (or the isosteric heat of adsorption) was also calculated from the average energies of the [MIL-88 + CO_2] system:

$$Q_{st} = [\langle U_{gh}\rangle - \langle U_h\rangle - \langle U_g\rangle] - RT. \quad (8)$$

where $\langle U_{gh}\rangle$, $\langle U_h\rangle$, and $\langle U_g\rangle$ are the average potential energy of the guest–host (CO_2 + MIL-88), the host (MIL-88), and the gas (CO_2), respectively.

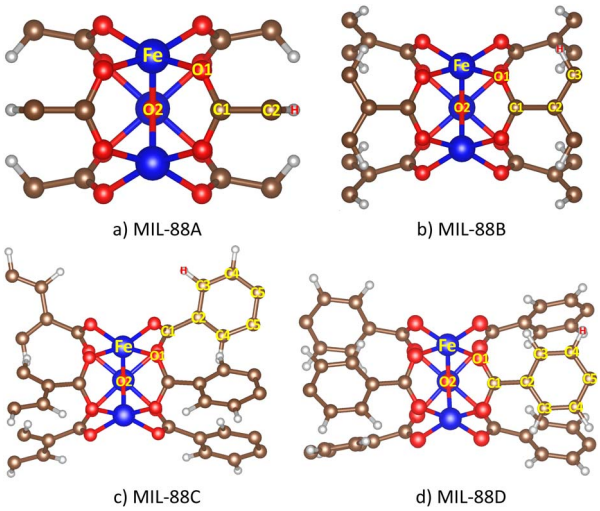

Fig. 2 The structure of MIL-88 series. Fe (blue), O (red), and C (brown), H (light-grey).

Table 1 The Lennard-Jones parameters, the atomic charges of the CO_2 molecule and the MIL-88 series[a]

Ions	ε/k_B (K)	σ (Å)	Partial charges (e^-)
Fe_MIL	6.54	2.59	1.222 (A), 1.212 (B), 1.208 (C), 1.306 (D)
H_MIL	7.65	2.85	0.118 (A), 0.099 (B), 0.096 (C, D)
C1_MIL	47.86	3.47	0.734 (A), 0.689 (B), 0.700 (C), 0.718 (D)
C2_MIL			−0.178 (A), −0.095 (B), −0.071 (C), −0.135 (D)
C3_MIL			−0.059 (B), −0.062 (C), −0.026 (D)
C4_MIL			−0.114 (C), −0.139 (D)
C5_MIL			0.058 (C), 0.073 (D)
O1_MIL	48.16	3.03	−0.570 (A, B), −0.574 (C), −0.603 (D)
O2_MIL (μ_3-O)			−0.875 (A), −0.844 (B), −0.849 (C), −0.939 (D)
C_CO_2 (ref. 41 and 42)	28.129	2.757	0.6512
O_CO_2 (ref. 41 and 42)	80.507	3.033	−0.3256

[a] μ_3-O: the oxygen atom at the center of the trimer of the MIL-88 series. The A, B, C, and D letters indicate MIL-88A, MIL-88B, MIL-88C, and MIL-88D, respectively.

3 Results and discussion

3.1. Adsorption configurations and energies

After optimizing the atomic positions of MIL-88s using the vdW-DF calculations, we loaded a CO_2 molecule into the MIL-88s structure to create the CO_2@MIL-88s systems, then continued fully relaxing their atomic positions. With many possibilities of the CO_2 adsorption sites on the Fe metal, the organic linker, and iron–oxygen hollow sites, see Fig. 3, we obtained the stable configurations of the CO_2 molecule and the corresponding adsorption energies. With three stable adsorption sites and two configurations (end-on and side-on) for each MOF, see Fig. 4 and Table 2, we found that there is a similarity among MIL-88A, B, and D that the side-on configuration is more stable than the end-on configuration on the hollow and linker, while the reverse tendency holds for the CO_2 molecule on the Fe metal. MIL-88C does not adsorb the CO_2 molecule on the linker. Even though the most favourable adsorption configuration of CO_2 is end-on on the Fe metal for MIL-88A, B, and C, while it is side-on on the linker for MIL-88D. We also observed that the CO_2 molecule adsorbed in the pore position among the metal site and the iron–oxygen hollow (see Fig. S2 in the ESI†). Therefore, the CO_2 molecule belongs to both the metal end-on and hollow end-on or metal side-on and hollow side-on configurations in MIL-88C. The bond distance from the CO_2 molecule to the nearest atoms of the MIL-88s is about 3 Å, Table 2. Besides, we found that the average adsorption strength of CO_2 at the favourable sites is in the order of MIL-88A (-37.52 kJ mol^{-1}) > MIL-88D (-19.33 kJ mol^{-1}) > MIL-88B (-14.25 kJ mol^{-1}) > MIL-88C (-2.9 kJ mol^{-1}). Notably, the adsorption of the CO_2 molecule is strongest and weakest on MIL-88A and C, respectively. The number of the favourable adsorption sites of MIL-88C is fewer than that of the others because its organic linker does not offer negative adsorption energy. A more detailed analysis revealed that the adsorption strength is MIL-88A (FMA linker) > MIL-88B (BDC linker) > MIL-88D (BPDC linker) > MIL-88C (NDC linker) for the metal, but it is MIL-88A > MIL-88D > MIL-88B > MIL-88C for the linker and hollow sites. The latter has the same tendency as the average adsorption energy. Also, the adsorption energy is significantly large on the linkers compared to the metal and hollow sites of MIL-88A, B, and D, which implies a significant role of the linkers.

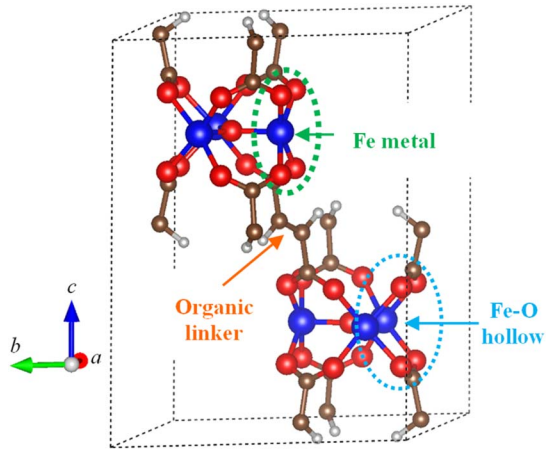

Fig. 3 The possible adsorption regions in a unit cell of MIL-88 series. Fe (blue), O (red), C (brown), and H (light-grey).

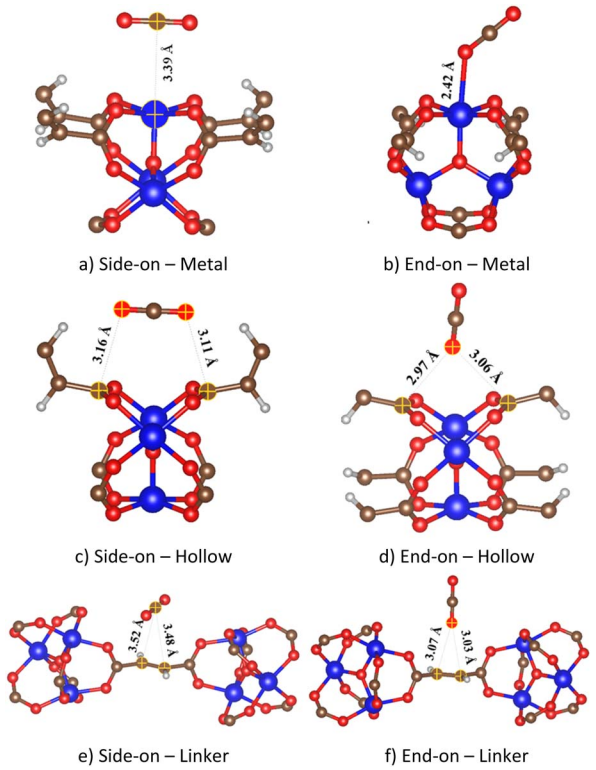

Fig. 4 The favorable CO_2 adsorption configurations in MIL-88A. Similarly, the CO_2 adsorption configuration in MIL-88B, C, and D was presented in the ESI (Fig. S1–S3).†

3.2. Electronic properties

The nature of the CO_2@MIL-88s interaction can be understood *via* the analysis of point charges, which were calculated by the Bader partition technique[43,44] and then excluded the neutral charge value of the corresponding atoms.[45,46] Table 3 shows that the C and O atoms of the CO_2 molecule always donate and accumulate the negative charge for all cases, respectively. However, the CO_2 molecule can gain (in most cases) or lose the charge. For MIL-88s, the Fe and C atoms always lose, while the O atoms always gain the negative charge. The charge of the H atoms of MIL-88s can vary depending on case by case, resulting in the total charge of MIL-88s, which can compensate for the charge losses or gains of the CO_2 molecule. Based on the obtained charge exchange of the CO_2 molecule and the MIL-88s, we found that the maximum value of the charge exchange of 11% e^- was achieved for the CO_2 adsorption with the side-on configuration at the Fe metal site in the MIL-88D. Therefore, the nature of the CO_2@MIL-88s interaction is the weak charge exchange.

The charge density difference in Fig. 5 shows that the charge accumulation and donation clouds of the CO_2 molecule have a relationship with that of the Fe and O atoms of the MIL-88

Table 2 Adsorption energy ΔE_{ads} (kJ mol^{-1}), the distance between the nearest atoms of CO_2 and MOF, d_{MIL-CO_2} (Å)

		MIL-88A		MIL-88B		MIL-88C		MIL-88D	
Site	Configuration	ΔE_{ads}	d_{MIL-CO_2}	ΔE_{ads}	d_{MIL-CO_2}	ΔE_{ads}	d_{MIL-CO_2}	ΔE_{ads}	d_{MIL-CO_2}
Metal	Side-on	−30.65	3.39	−0.46	3.37	−0.870[a]	3.36	−12.73	3.42
	End-on	**−57.88**	2.42	**−37.23**	2.38	**−4.962**[b]	2.33	−24.96	2.44
Hollow	Side-on	−28.59	3.16, 3.11	−6.87	3.08, 3.09	−0.870[a]	3.58, 3.36	−20.84	3.17, 3.19
	End-on	−20.62	2.97, 3.06	−6.26	3.49, 3.67	**−4.962**[b]	3.22, 3.17	−11.01	2.99, 3.01
Linker	Side-on	−45.16	3.48, 3.52	−15.55	3.57, 3.58	—	—	**−26.88**	3.39, 3.45
	End-on	−42.23	3.03, 3.07	−5.36	3.44, 3.57	—	—	−19.57	3.27, 3.27
Average adsorption energy		−37.52		−11.96		−2.916		−19.33	

[a] These adsorption configurations are identical. [b] These adsorption configurations are identical.

Table 3 The Bader charge transfer (e$^-$) between the CO_2 molecule and the MIL-88 series. Positive and negative values implied the negative charge (e$^-$) accumulation and donation, respectively

		Metal		Hollow		Linker	
Site/configuration		Side-on	End-on	Side-on	End-on	Side-on	End-on
CO_2@MIL-88A	1C	−1.949	−2.071	−1.995	−2.013	−2.074	−2.057
	2O	1.954	2.097	2.059	2.065	2.100	2.068
	CO_2	**0.006**	**0.025**	**0.065**	**0.052**	**0.026**	**0.011**
	12H	0.132	0.068	−0.013	0.073	0.146	0.129
	24C	−19.016	−18.923	−18.892	−18.996	−19.069	−19.029
	26O	27.221	27.239	27.360	27.269	27.340	27.315
	6Fe	−8.343	−8.409	−8.382	−8.398	−8.443	−8.426
	MIL-88A	**−0.006**	**−0.025**	**−0.065**	**−0.052**	**−0.026**	**−0.011**
CO_2@MIL-88B	1C	−2.072	−2.064	−1.966	−1.983	−2.055	−2.070
	2O	2.080	2.053	1.973	1.991	2.085	2.098
	CO_2	**0.008**	**−0.011**	**0.007**	**0.008**	**0.030**	**0.028**
	24H	−0.186	0.093	−0.101	−0.110	−0.172	−0.239
	48C	−18.771	−18.945	−18.910	−18.894	−18.727	−18.785
	26O	27.356	27.296	27.424	27.369	27.300	27.431
	6Fe	−8.407	−8.434	−8.420	−8.374	−8.431	−8.436
	MIL-88B	**−0.008**	**0.011**	**−0.007**	**−0.008**	**−0.030**	**−0.028**
CO_2@MIL-88C	1C	−2.021			−2.090		
	2O	2.039			2.069		
	CO_2	**0.018**			**−0.021**		
	36H	0.316			0.263		
	72C	−19.275			−19.286		
	26O	27.166			27.288		
	6Fe	−8.225			−8.245		
	MIL-88C	**−0.018**			**0.021**		
CO_2@MIL-88D	1C	−1.935	−2.029	−1.943	−1.999	−1.974	−2.050
	2O	2.045	2.014	1.951	2.006	1.994	2.076
	CO_2	**0.110**	**−0.016**	**0.008**	**0.007**	**0.020**	**0.026**
	48H	0.256	0.249	0.207	0.228	0.117	0.220
	85C	−19.288	−19.248	−19.331	−19.385	−19.160	−19.248
	26O	27.340	27.427	27.556	27.549	27.440	27.416
	6Fe	−8.418	−8.413	−8.440	−8.399	−8.417	−8.414
	MIL-88D	**−0.110**	**0.016**	**−0.008**	**−0.007**	**−0.020**	**−0.026**

series, while the C and H atoms of the MIL-88 series exhibit an ignorable role in the interaction with the CO_2 molecule as no significant charge clouds have been found on these atoms. Besides, we explored the nature of the CO_2@MIL-88s interaction at the electronic orbital level through the analysis of the orbital-projected density of states (PDOS), which was presented in Fig. 6. This figure revealed that the $1\pi_g$, $2\sigma_u/1\pi_u$, and $2\sigma_g$ peaks of the CO_2 molecule locate near −4.5, −8.0, and −9.5 eV, respectively.[47] The p_x, p_y, p_z, and s orbitals of the MIL-88 series distribute below −1.0 eV, while the d orbitals of the MIL-88s position around the Fermi level. Generally, the interaction between adsorbate and adsorbent stems from the attraction between occupied states of the isolated adsorbate with unoccupied states of the isolated adsorbent and *vice versa*. When the

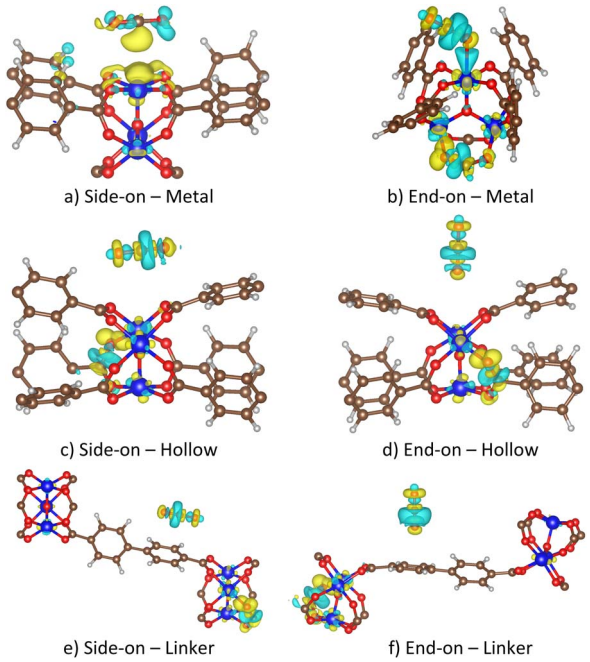

Fig. 5 The charge density difference of the CO_2@MIL-88D system with the different adsorption configurations and sites. Negative charge accumulation (yellow) and donation (cyan). Similar features of the charge clouds have been shown for MIL-88A, B, and C in Fig. S4–S6 in the ESI.† Isosurface values (e^- $bohr^{-3}$) for the charge density difference of the MIL-88D@CO_2 system at different sites are listed in Table S1.†

combined system is formed, the electronic states of the adsorbate and the adsorbent become completely overlapping to make the peak resonance. Therefore, the overlapping between the electronic states of the adsorbate and adsorbent becomes an indication of their interaction. We found in Fig. 6 that the peak resonance forms between the DOS peaks of the CO_2 molecule with mainly the C and O p_x, p_y, and p_z orbitals and weakly the Fe s and d_{z^2} orbitals of the MIL-88 series for the energy below −1.0 eV. This observation and the charge density difference implied that the C and O p_x, p_y, and p_z orbitals of the organic linkers should be the dominant factors contributing to the CO_2@MIL-88s interaction.

3.3. The CO_2 capture capacity of MIL-88 series

Using the force fields presented in the Computational techniques section, we calculated the CO_2 capture gravimetric and volumetric capacities of the MIL-88 series *via* the isotherms as a function of pressures at the temperature of 298 K. Fig. 7a displays the obtained isotherms in gravimetric uptake, *i.e.*, the adsorbed amount per unit mass of adsorbent (wt%), and Fig. 7b is in volumetric uptakes, *i.e.*, the adsorbed amount per unit volume (cm^3 (STP) per cm^3). Besides, the number of CO_2 molecules loading per unit cell of MIL-88A, MIL-88B, MIL-88C, and MIL-88D were also displayed in Fig. S8 in ESI.† We found that the total and excess isotherms rapidly increase at the low-pressure range and gradually enhance with the increase in pressure. Afterward, the excess isotherms approach their maximum value[48,49] and slowly decrease after passing by the

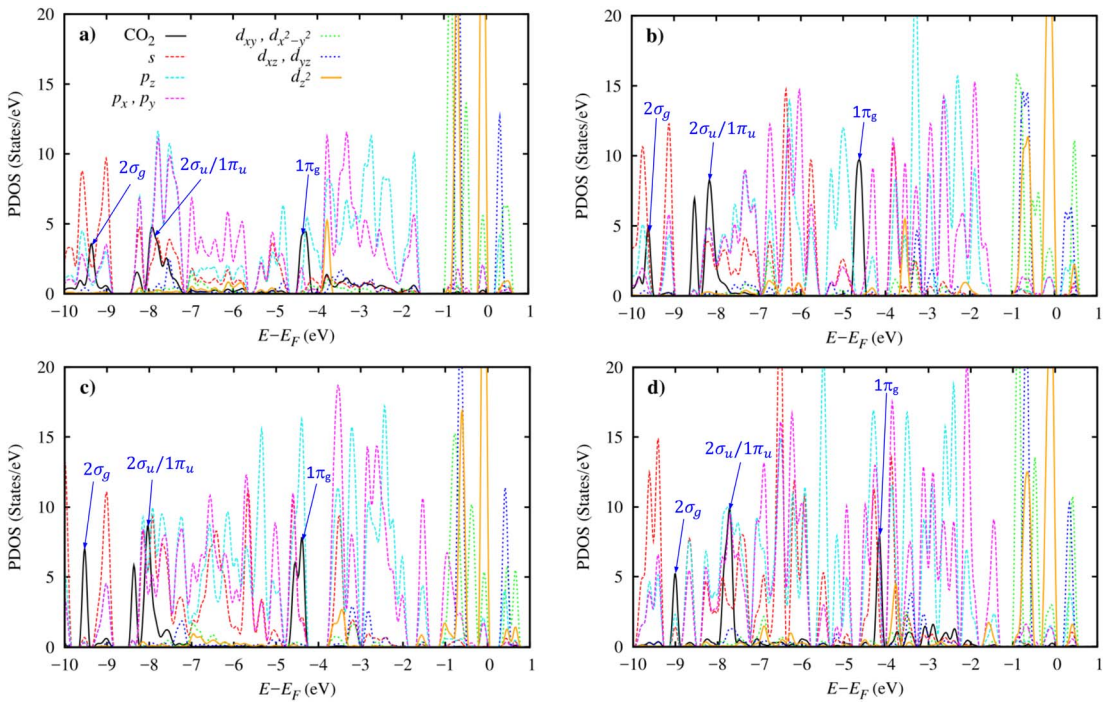

Fig. 6 The orbital-projected density of states of the CO_2@MIL-88 systems in the most favourable adsorption state: (a) end-on at the Fe metal of MIL-88A, (b) end-on at the Fe metal of MIL-88B, (c) end-on at the Fe metal of MIL-88C, and (d) side-on at the organic linker of MIL-88D. The Fermi level was set to 0 eV.

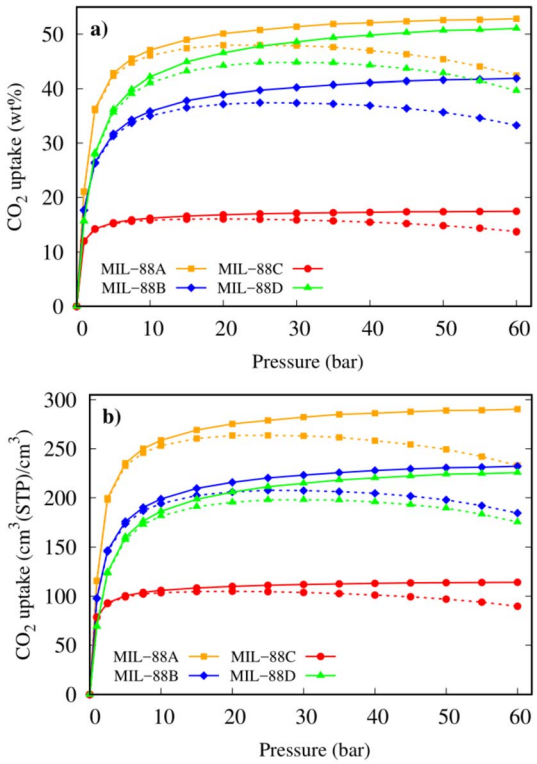

Fig. 7 The excess (dashed line) and total (solid line) CO_2 adsorption isotherms of MIL-88A, B, C, and D at 298 K: (a) gravimetric capacity and (b) volumetric capacity.

Table 4 The maximum excess and absolute capture capacity of CO_2 in MIL-88A, B, C, and D at 298 K

	mmol g^{-1}		wt%		cm^3 (STP) per cm^3	
Adsorbent	Total	Excess	Total	Excess	Total	Excess
MIL-88A	12.11	10.90	53.26	47.98	292.65	263.61
MIL-88B	9.61	8.51	42.29	37.45	234.44	207.60
MIL-88C	4.00	3.64	17.58	16.04	115.11	104.98
MIL-88D	11.74	10.18	51.66	44.79	228.35	197.97

maximum while the total isotherms continue developing up to 60 bar. Table 4 lists the maximal CO_2 uptakes for gravimetric and volumetric capacities, where maximum excess loading was achieved at 25 bar for MIL-88A and B, 20 bar for MIL-88C, and 30 bar for MIL-88D. The highest value of total uptake was achieved at 60 bar for MIL-88A, B, and D, while it reached the earlier pressure value, about 20 bar for MIL-88C because the isotherms become flat for pressures greater than 20 bar. Table 4 shows that both excess and total isotherms are in the order MIL-88A (FMA linker) > MIL-88D (BPDC linker) > MIL-88B (BDC linker) > MIL-88C (NDC linker) for the gravimetric CO_2 uptake (proportional to the adsorption energy tendency at the linker and hollow sites) and MIL-88A > MIL-88B > MIL-88D > MIL-88C (proportional to the adsorption energy tendency at the metal site) for the volumetric uptake. This finding implies that MIL-88A and MIL-88C would be the best and worst candidates for CO_2 capture, respectively. Also, the tendency of the gravimetric uptakes is in good agreement with that of the average adsorption energy obtained above, *i.e.*, the stronger the adsorption energy, the higher the capture capacity.

Next, we calculated the isosteric heat of the CO_2 adsorption, Q_{st}, in MIL-88s, as shown in Fig. 8. The average value of the curves exhibited Q_{st} in the order: MIL-88A (34.9 kJ mol^{-1}) > MIL-88B (32.5 kJ mol^{-1}) > MIL-88D (32.1 kJ mol^{-1}) > MIL-88C (31.8 kJ mol^{-1}). This tendency is consistent with the volumetric uptakes and the adsorption energy at the metal site, as mentioned above. Moreover, the value of Q_{st} represents the CO_2@MIL-88s interaction. The obtained values of Q_{st} are rather high compared to those of many other MOFs.[50]

To elucidate the effect of moisture on the CO_2 adsorption capacity in the MIL-88 series, we calculated both gravimetric and volumetric amounts of CO_2 adsorption in the presence of H_2O. The results were described in Fig. S7 and Table S2 in ESI.† Compared to those without H_2O, the CO_2 adsorption capacities in MIL-88s insignificantly decreased in the presence of H_2O. The decrease was about 4–8% for the absolute uptakes at 40 bar and 2–6% for the maximum excess.

It is necessary to consider the influences of macroscopic parameters on the CO_2 capture capacity. Fig. 9 presents the dependence of the gravimetric uptakes of the CO_2 capture on the specific surface area and pore volume of the MIL-88 series. We found a simple relationship, *i.e.*, adsorption capacity proportionally depends on the specific surface area (Fig. 9a) and the pore volume (Fig. 9b). Here, the specific surface area and pore volume data of the MIL-88 series were calculated theoretically by grand canonical Monte Carlo simulations with nitrogen gas utilized to obtain them.

Substituting the organic linkers caused the effects on adsorption energy and uptakes, which were perhaps due to the following reasons: (1) geometric modification, *i.e.*, the organic linkers led to the different SSA and pore volume of MIL-88s. The larger SSA and pore volume lead to higher CO_2 capacity. (2) Electronic property modification *via* the overlapping of wavefunctions[22] between CO_2 and the organic linkers, even for the metal and hollow adsorption sites, see Fig. S9 in ESI.† We found that the wavefunctions of CO_2 and that of the C and O atoms of

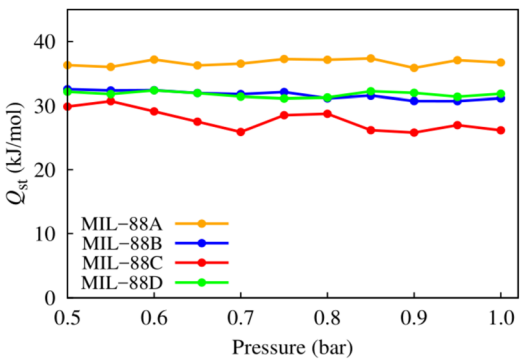

Fig. 8 The isosteric heat of the CO_2 adsorption in MIL-88 series at the low-pressure range and 298 K.

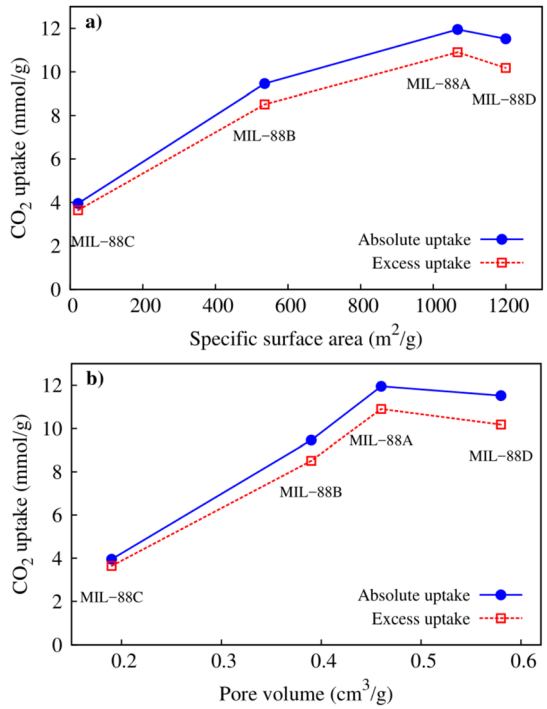

Fig. 9 The relationship between the CO_2 uptakes with (a) specific surface area and (b) pore volume.

the organic linkers can overlap. The same or opposite direction oscillations of the wavefunctions cause constructive and destructive interferences, respectively. We can see that the wavefunction interaction of CO_2 with the organic linker shows more clearly for MIL-88A and D than for MIL-88B and C, which somehow shows a relationship to the obtained CO_2 uptakes.

Fig. 10 shows the excess gravimetric capacity of CO_2 *versus* temperature at a low pressure of 1 bar. The uptake decreases as the temperature increases, following the straight line for MIL-88C; however, the curves for MIL-88A, B, and D. The isotherms approach a convergent value as the temperature is high enough from the room temperature. Particularly, MIL-88A achieved the excess uptake of 4.00 mmol g^{-1} at 303 K, which is in good agreement with the experimental value of 4.95 mmol g^{-1} at 30 °C (303 K).[25] Moreover, the shape of the CO_2 adsorption curve on MIL-88A is consistent with that of the experiment in the temperature range from 293 to 333 K.[25]

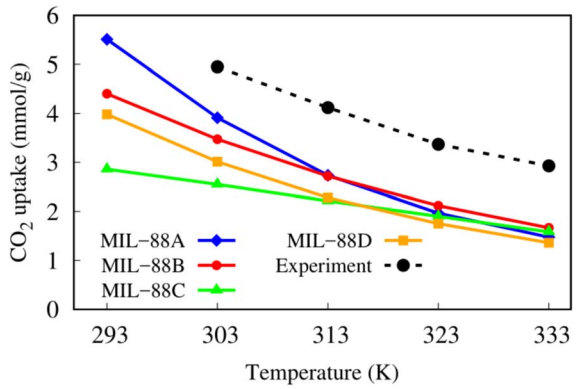

Fig. 10 The excess uptakes *versus* temperatures of MIL-88 series at 1 bar. The experimental data were obtained from ref. 25.

4 Conclusions

This work investigated the CO_2@MIL-88s interaction and the CO_2 capture capacity in the MIL-88 series using the vdW-DF density functional theory calculations and grand canonical Monte Carlo simulations. We found a proportional relationship between the adsorption energy with the gravimetric uptake FMA linker (MIL-88A) > BPDC linker (MIL-88D) > BDC linker (MIL-88B) > NDC linker (MIL-88C), proportional to the adsorption strength of CO_2 at the linker and hollow sites and the isosteric heat of CO_2 adsorption with the volumetric uptake FMA linker (MIL-88A) > BDC linker (MIL-88B) > BPDC linker (MIL-88D) > NDC linker (MIL-88C), proportional to the adsorption strength of CO_2 at the metal site). We have to emphasize that the replacement of the organic linkers is the only difference in the geometric structure of MIL-88A, B, C, and D. Therefore, the substitution of the linkers also influences the adsorption strength of CO_2 not only at the organic linkers but also at the metal and hollow sites. The gravimetric and volumetric uptakes indicated that MIL-88A (with fumarate linker) should be the best candidate among the MIL-88 series for CO_2 capture. Furthermore, the physical insights have been elucidated that the contributions of the MIL-88 series to the interaction with CO_2 are as follows: the C and O p orbitals (dominant) and the Fe s and d_{z^2} orbitals (minor). The H atoms of the MIL-88 series played an ignorable role in the CO_2@MIL-88 interaction.

Author contributions

Conceptualization (DNS, VC), formal analysis (NTXH, DNS), investigation (NTXH, DNS), resources (DNS, VC), supervision (DNS), validation (NTXH, VC, DNS), visualization (NTXH, OKL, TPD), writing of original draft (DNS), reviewing and editing (VC, DNS).

Conflicts of interest

There are no conflicts of interest to declare.

Acknowledgements

This research is funded by Vietnam National University Ho Chi Minh City (VNU-HCM) under grant number VL2022-20-01.

References

1 K. Sumida, D. L. Rogow, J. A. Mason, T. M. McDonald, E. D. Bloch, Z. R. Herm, T. H. Bae and J. R. Long, A short review of recent advances in CO_2 hydrogenation to hydrocarbons over heterogeneous catalysts, *Chem. Rev.*, 2012, **112**, 724–781.

2 R. Quadrelli and S. Peterson, The energy-climate challenge: recent trends in CO_2 emissions from fuel combustion, *Energy Policy*, 2007, **35**, 5938–5952.
3 S. E. M. Elhenawy, M. Khraisheh, F. Almomani and G. Walker, Metal-organic frameworks as a platform for CO_2 capture and chemical processes: adsorption, membrane separation, catalytic-conversion, and electrochemical reduction of CO_2, *Catalysts*, 2020, **10**, 1–33.
4 M. Kanniche, R. Gros-Bonnivard, P. Jaud, J. Valle-Marcos, J. M. Amann and C. Bouallou, Pre-combustion, post-combustion and oxy-combustion in thermal power plant for CO_2 capture, *Appl. Therm. Eng.*, 2010, **30**, 53–62.
5 A. Rehman, S. Farrukh, A. Hussain and E. Pervaiz, Synthesis and effect of metal–organic frame works on CO_2 adsorption capacity at various pressures: a contemplating review, *Energy Environ.*, 2020, **31**, 367–388.
6 D. Y. C. Leung, G. Caramanna and M. M. Maroto-valer, An overview of current status of carbon dioxide capture and storage technologies, *Renew. Sust. Energ. Rev.*, 2014, **39**, 426–443.
7 J. Y. Jung, F. Karadas, S. Zulfiqar, E. Deniz, S. Aparicio, M. Atilhan, C. T. Yavuz and S. M. Han, Limitations and high pressure behavior of MOF-5 for CO2 capture, *Phys. Chem. Chem. Phys.*, 2013, **15**, 14319–14327.
8 W. S. Drisdell, R. Poloni, T. M. McDonald, T. A. Pascal, L. F. Wan, C. Das Pemmaraju, B. Vlaisavljevich, S. O. Odoh, J. B. Neaton, J. R. Long, D. Prendergast and J. B. Kortright, Probing the mechanism of CO2 capture in diamine-appended metal-organic frameworks using measured and simulated X-ray spectroscopy, *Phys. Chem. Chem. Phys.*, 2015, **17**, 21448–21457.
9 Y. Li, H. Xu, S. Ouyang and J. Ye, Metal-organic frameworks for photocatalysis, *Phys. Chem. Chem. Phys.*, 2016, **18**, 7563–7572.
10 S. Kang and J. Yu, Electronic structure and magnetic properties of transition metal Kagome metal-organic frameworks, *Phys. Chem. Chem. Phys.*, 2022, **24**, 22168–22180.
11 A. J. Howarth, Y. Liu, P. Li, Z. Li, T. C. Wang, J. T. Hupp and O. K. Farha, Chemical, thermal and mechanical stabilities of metal-organic frameworks, *Nat. Rev. Mater.*, 2016, **1**, 1–15.
12 T. T. T. Huong, P. N. Thanh, N. T. X. Huynh and D. N. Son, Metal – organic frameworks: state-of-the-art material for gas capture and storage, *VNU J. Sci. Math. –Phys.*, 2016, **32**, 67–85.
13 H. Furukawa, N. Ko, Y. B. Go, N. Aratani, S. B. Choi, E. Choi, A. O. Yazaydin, R. Q. Snurr, M. O'Keeffe, J. Kim and O. M. Yaghi, Ultrahigh porosity in metal-organic frameworks, *Science*, 2010, **329**, 424–428.
14 A. R. Millward and O. M. Yaghi, Metal-organic frameworks with exceptionally high capacity for storage of carbon dioxide at room temperature, *J. Am. Chem. Soc.*, 2005, **127**, 17998–17999.
15 P. L. Llewellyn, S. Bourrelly, C. Serre, A. Vimont, M. Daturi, L. Hamon, G. De Weireld, J. Chang, D. Hong, Y. K. Hwang and S. H. Jhung, High uptakes of CO_2 and CH_4 in mesoporous metal-organic frameworks MIL-100 and MIL-101, *Langmuir*, 2008, **24**, 7245–7250.
16 C. Dey, *et al.*, Crystalline metal-organic frameworks (MOFs): synthesis, structure and function, *Acta Crystallogr., Sect. B: Struct. Sci., Cryst. Eng. Mater.*, 2014, **70**, 3–10.
17 P. Horcajada, F. Salles, S. Wuttke, T. Devic, D. Heurtaux, A. Vimont, M. Daturi, O. David, E. Magnier, N. Stock, Y. Filinchuk, D. Y. Popov, C. Riekel, G. Férey, C. Serre, G. Maurin and D. Popov, How linker's modification controls swelling properties of highly flexible iron (III) dicarboxylates MIL-88, *J. Am. Chem. Soc.*, 2011, **133**, 17839–17847.
18 J. Wang, J. Wan, Y. Ma, Y. Wang, M. Pu and Z. Guan, Metal–organic frameworks MIL-88A with suitable synthesis conditions and optimal dosage for effective catalytic degradation of Orange G through persulfate activation, *RSC Adv.*, 2016, **6**, 112502–112511.
19 W.-T. Xu, L. Ma, F. Ke, F.-M. Peng, G.-S. Xu, Y.-H. Shen, J.-F. Zhu, L.-G. Qiu and Y.-P. Yuan, Metal-organic frameworks MIL-88A hexagonal microrods as a new photocatalyst for efficient decolorization of methylene blue dye, *Dalton Trans.*, 2014, **43**, 3792–3798.
20 A. C. McKinlay, J. F. Eubank, S. Wuttke, P. S. Wheatley, P. Bazin, J.-C. Lavalley, M. Daturi, A. Vimont, G. De Weireld, P. Horcajada, C. Serre and R. E. Morris, Nitric oxide adsorption and delivery in flexible MIL-88(Fe) metal− organic frameworks, *Chem. Mater.*, 2013, **25**, 1592–1599.
21 S. N. Kim, C. G. Park, B. K. Huh, S. H. Lee, C. H. Min, Y. Y. Lee, Y. K. Kim, K. H. Park and Y. B. Choy, Metal-organic frameworks, NH2-MIL-88(Fe), as carriers for ophthalmic delivery of brimonidine, *Acta Biomater.*, 2018, **79**, 344–353.
22 N. T. X. Huynh, O. M. Na, V. Chihaia and D. N. Son, A computational approach towards understanding hydrogen gas adsorption in Co-MIL-88A, *RSC Adv.*, 2017, **7**, 39583–39593.
23 N. T. X. Huynh, V. Chihaia and D. N. Son, Hydrogen storage in MIL-88 series, *J. Mater. Sci.*, 2019, **54**, 3994–4010.
24 N. T. X. Huynh, V. Chihaia and D. N. Son, Enhancing hydrogen storage by metal substitution in MIL-88A metal-organic framework, *Adsorption*, 2020, **26**, 509–519.
25 S. Wongsakulphasatch, W. Kiatkittipong, J. Saupsor, J. Chaiwiseshphol, P. Piroonlerkgul, V. Parasuk and S. Assabumrungrat, Effect of Fe open metal site in metal-organic frameworks on post-combustion CO2 capture performance, *Greenhouse Gases: Sci. Technol.*, 2016, **7**, 383–394.
26 C. Serre, F. Millange, S. Surblé and G. Férey, A route to the synthesis of trivalent transition-metal porous carboxylates with trimeric secondary building units, *Angew. Chem., Int. Ed.*, 2004, **43**, 6286–6289.
27 S. Surblé, C. Serre, C. Mellot-Draznieks, F. Millange and G. Férey, A new isoreticular class of metal-organic-frameworks with the MIL-88 topology, *Chem. Commun.*, 2006, 284–286.

28 J. P. Perdew, J. Chevary, S. Vosko, K. Jackson, M. Pederson, D. Singh and C. Fiolhais, Atoms, molecules, solids, and surfaces: applications of the generalized gradient approximation for exchange and correlation, *Phys. Rev. B: Condens. Matter Mater. Phys.*, 1992, **46**, 6671–6687.

29 J. P. Perdew, K. Burke and M. Ernzerhof, Generalized gradient approximation made simple, *Phys. Rev. Lett.*, 1996, **77**, 3865–3868.

30 G. Kresse and J. Furthmüller, Efficient iterative schemes for ab initio total-energy calculations using a plane-wave basis set, *Phys. Rev. B: Condens. Matter Mater. Phys.*, 1996, **54**, 11169–11186.

31 G. Kresse and J. Furthmüller, Efficiency of ab initio total energy calculations for metals and semiconductors using a plane-wave basis set, *Comput. Mater. Sci.*, 1996, **6**, 15–50.

32 P. E. Blöchl, Projector augmented-wave method, *Phys. Rev. B: Condens. Matter Mater. Phys.*, 1994, **50**, 17953–17979.

33 G. Kresse and D. Joubert, From ultrasoft pseudopotentials to the projector augmented-wave method, *Phys. Rev. B: Condens. Matter Mater. Phys.*, 1999, **59**, 1758–1775.

34 M. Methfessel and A. T. Paxton, High-precision sampling for Brillouin-zone integration in metals, *Phys. Rev. B: Condens. Matter Mater. Phys.*, 1989, **40**, 3616–3621.

35 P. E. Blochl, O. Jepsen and O. K. Andersen, Improved tetrahedron method for Brillouin-zone integrations, *Phys. Rev. B: Condens. Matter Mater. Phys.*, 1994, **49**, 16223–16233.

36 T. A. Manz and N. G. Limas, Introducing DDEC6 atomic population analysis: Part 1. Charge partitioning theory and methodology, *RSC Adv.*, 2016, **6**, 47771–47801.

37 N. G. Limas and T. A. Manz, Introducing DDEC6 atomic population analysis: Part 2. Computed results for a wide range of periodic and nonperiodic materials, *RSC Adv.*, 2016, **6**, 45727–45747.

38 T. A. Manz, Introducing DDEC6 atomic population analysis: part 3. Comprehensive method to compute bond orders, *RSC Adv.*, 2017, **7**, 45552–45581.

39 N. G. Limas and T. A. Manz, Introducing DDEC6 atomic population analysis: part 4. Efficient parallel computation of net atomic charges, atomic spin moments, bond orders, and more, *RSC Adv.*, 2018, **8**, 2678–2707.

40 D. Dubbeldam, S. Calero, D. E. Ellis and R. Q. Snurr, RASPA: molecular simulation software for adsorption and diffusion in flexible nanoporous materials, *Mol. Simul.*, 2016, **42**, 81–101.

41 J. G. Harris and K. H. Yungt, Carbon dioxide's liquid-vapor coexistence curve and critical properties as predicted by a simple molecular model, *J. Phys. Chem.*, 1995, **99**, 12021–12024.

42 K. Makrodimitris, G. K. Papadopoulos and D. N. Theodorou, Prediction of permeation properties of CO_2 and N_2 through silicalite via molecular simulations, *J. Phys. Chem. B*, 2001, **105**, 777–788.

43 G. Henkelman, A. Arnaldsson and H. Jónsson, A fast and robust algorithm for Bader decomposition of charge density, *Comput. Mater. Sci.*, 2006, **36**, 354–360.

44 W. Tang, E. Sanville and G. Henkelman, A grid-based Bader analysis algorithm without lattice bias, *J. Phys.: Condens. Matter*, 2009, **21**(7), 084204.

45 O. K. Le, V. Chihaia, P. T. H. Hoa, P. T. Hai and D. N. Son, Physical insights into the Au growth on the surface of a $LaAlO_3/SrTiO_3$ heterointerface, *RSC Adv.*, 2022, **12**, 24146–24155.

46 O. K. Le, V. Chihaia, V. V. On and D. N. Son, N-type and p-type molecular doping on monolayer MoS_2, *RSC Adv.*, 2021, **11**, 8033–8041.

47 D. N. Son, T. T. T. Huong and V. Chihaia, Simultaneous adsorption of SO_2 and CO_2 in an $Ni(bdc)(ted)_{0.5}$ metal-organic framework, *RSC Adv.*, 2018, **8**, 38648–38655.

48 K. S. Walton, A. R. Millward, D. Dubbeldam, H. Frost, J. J. Low, O. M. Yaghi and R. Q. Snurr, Understanding inflections and steps in carbon dioxide adsorption isotherms in metal-organic frameworks, *J. Am. Chem. Soc.*, 2008, **130**, 406–407.

49 M. Gheytanzadeh, A. Baghban, S. Habibzadeh, A. Esmaeili, O. Abida, A. Mohaddespour and M. T. Munir, Towards estimation of CO_2 adsorption on highly porous MOF-based adsorbents using Gaussian process regression approach, *Sci. Rep.*, 2021, **11**, 1–13.

50 Z. Li, P. Liu, C. Ou and X. Dong, Porous metal-organic frameworks for carbon dioxide adsorption and separation at low pressure, *ACS Sustainable Chem. Eng.*, 2020, **8**, 15378–15404.